ResearchGate

See discussions, stats, and author profiles for this publication at: https://www.researchgate.net/publication/321400804

Orbital error modeling and analysis of spaceborne InSAR

Conference Paper · November 2017

DOI: 10.1109/BIGSARDATA.2017.8124930

CITATIONS
3

READS
149

3 authors:

Xue Chen
University of Padova
11 PUBLICATIONS **121** CITATIONS
SEE PROFILE

Junhuan Peng
68 PUBLICATIONS **701** CITATIONS
SEE PROFILE

Honglei Yang
China University of Geosciences (Beijing)
43 PUBLICATIONS **433** CITATIONS
SEE PROFILE

All content following this page was uploaded by Xue Chen on 07 July 2023.

The user has requested enhancement of the downloaded file.

ORBITAL ERROR MODELING AND ANALYSIS OF SPACEBORNE INSAR

Xue Chen Junhuan Peng Honglei Yang*

School of Land Science and Technology, China University of Geosciences, Beijing, China
No.29 Xueyuan Road, Haidian District

ABSTRACT

Spaceborne synthetic aperture radar interferometry is a key earth observation technique for large-area deformation monitoring. Measurements can be biased by error originating from different sources. Satellite orbital error affects interferograms in the form of an almost linear signal. The commonly used methods to mitigate the orbital error are to calculate the residual baseline error by the Fast Fourier Transform on the residual phase or to fit it with the quadratic surface. These two methods are applicable in most cases, but do not apply in the presence of a large-scale deformation signal that has similar spatial characteristics, such as tectonic movement or tides. Based on the current research on modeling and analysis of baseline error, this paper realized the orbital error network adjustment of Envisat ASAR data in Los Angeles area according to the principle of network adjustment. For quality control on the network level, iterative data snooping has been used, and the result proved its capability to detect and reject outliers.

Index Terms—Synthetic Aperture Radar Interferometry, Baseline Estimation, Orbital Error, Network Adjustment

1. INTRODUCTION

Synthetic Aperture Radar Interferometry (InSAR) is an earth observation technique to obtain the elevation data or surface deformation information base on two or more than two times imaging of a radar satellite in the same area. InSAR technique has played an important role in the study of surface deformation, ground subsidence, landslides, glaciers, volcanoes [1] and so on. Differential Synthetic Aperture Radar Interferometry (D-InSAR) can obtain the phase difference with high accuracy, which can't reflect deformation phase directly as it may be influenced by imprecise orbit state vector, atmospheric delay during electromagnetic wave propagation and Digital Elevation Model(DEM) error. Orbital error affects the accuracy of InSAR technique significantly. Firstly, small orbital error may propagate to interferograms causing obvious residual phase. Secondly, influence factors like atmospheric propagation delay phase, deformation phase, DEM error and random error are inevitable. The time series InSAR technique such as Persisrent Scatterers InSAR [2][3][4] and Small Baseline Subsets InSAR [5] can detect linear and nonlinear deformation, and eliminate the effect of orbital error in theory, but in data processing, the influence of orbital error on phase unwrapping and elevation phase can't be ignored. Therefore, it is necessary to model and analyze the orbital error.

Since Graham [6] proposed the concept of InSAR 3D imaging in 1974, many countries and institutions had begun to study InSAR technique. Orbital error is considered to be the main limiting factor for long wavelength displacement measurement by InSAR technique [7].

Li and Goldstein [8] have proved that InSAR can be used to measure topography. Many methods have been taken to mitigate the orbital error. Some simple methods have been proposed such as fitting inteferometric phase with linear or two quadric surface [9][10], reestimating baseline, and calculating the fringes caused by orbital error. More accurate methods are making consistent estimation of phase fitting surface [9], or making compensation to orbits[11][12]. Zhang et al. [13] proposed a model for joint estimation of deformation rates and orbital error from multitemporal interferograms without unwrapping. Liu et al. [14] established a nonlinear error model for the InSAR baseline. Bähr and Hanssen [12] proposed reliable and rigorous geometric modeling of the orbital error signal, and systematic biases can be detected and iteratively eliminated.

2. METHODOLOGY

2.1. Baseline Error Estimation

Various method of estimating baseline error has been concluded by Bähr [15]. He has described the effect of an baseline error components yielding a distinct inteferometric signal (see Figure 1). Here, we choose the least square estimation to obtain baseline error [15][16].

Reference phase is caused by the difference between sensors and ground object [17]. The bias of range between master satellite and ground object and range between slave satellite and ground object is regarded as orbital error. Thus, orbital error can be expressed by the equation :

$$E\{\varphi\} = \delta\phi_{\mathrm{orb}} = -\delta\phi_{\mathrm{ref}} = \frac{4\pi}{\lambda}\left(\delta R_{\mathrm{M,ref}} - \delta R_{\mathrm{S,ref}}\right) + \varphi_0 \quad (1)$$

978-1-5386-4519-2/17/$31.00 ©2017 IEEE

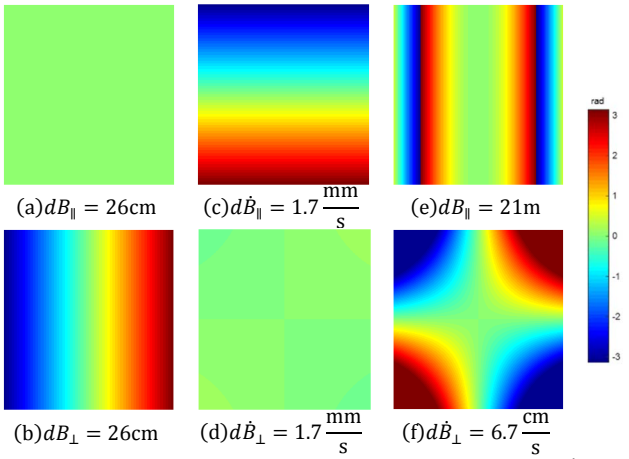

(a)$dB_{\parallel} = 26\text{cm}$ (c)$d\dot{B}_{\parallel} = 1.7\frac{\text{mm}}{\text{s}}$ (e)$dB_{\parallel} = 21\text{m}$

(b)$dB_{\perp} = 26\text{cm}$ (d)$d\dot{B}_{\perp} = 1.7\frac{\text{mm}}{\text{s}}$ (f)$d\dot{B}_{\perp} = 6.7\frac{\text{cm}}{\text{s}}$

Figure 1 Baseline Error Components $dB_{\perp}$ and $\dot{B}_{\parallel}$

φ_0 is the relative bias constant. After a series of complex mathematical operations, considering N pixels, baseline error parameter $\boldsymbol{b}^T = \begin{pmatrix}\delta B_h & \delta \dot{B}_h & \delta B_v & \delta \dot{B}_v\end{pmatrix}$ can be estimated by the function model :

$$E\{\varphi\} = \begin{pmatrix} \vdots & \vdots & \vdots & \vdots \\ a_{h,i} & a_{h,i}t_i & a_{v,i} & a_{v,i}t_i \\ \vdots & \vdots & \vdots & \vdots \end{pmatrix} \begin{pmatrix} \delta B_h \\ \delta \dot{B}_h \\ \delta B_v \\ \delta \dot{B}_v \end{pmatrix} + \begin{pmatrix} \varphi_0 \\ \varphi_0 \\ \varphi_0 \\ \varphi_0 \end{pmatrix}$$

$$=: \boldsymbol{A}_b \boldsymbol{b} + \boldsymbol{1}\varphi_0 \quad (2)$$

Stochastic model:

$$D\{\varphi\} = \sigma_0^2 \boldsymbol{Q}_{\varphi} \quad (3)$$

The equation is solved by least square estimation [15].

$$\widehat{\boldsymbol{b}}_{\theta} = \left(\boldsymbol{T}\overline{\boldsymbol{A}}_b^T \boldsymbol{Q}_{\varphi}^{-1} \overline{\boldsymbol{A}}_b \boldsymbol{T}^T\right)^{-1} \boldsymbol{T}\overline{\boldsymbol{A}}_b^T \boldsymbol{Q}_{\varphi}^{-1} \varphi \quad (4)$$

$$D\{\widehat{\boldsymbol{b}}_{\theta}\} = \sigma_0^2 \boldsymbol{Q}_{\theta} = \sigma_0^2 \left(\boldsymbol{T}\overline{\boldsymbol{A}}_b^{\mathrm{T}} \boldsymbol{Q}_{\varphi}^{-1} \overline{\boldsymbol{A}}_b \boldsymbol{T}^{\mathrm{T}}\right)^{-1} \quad (5)$$

With $\boldsymbol{b}_{\theta}^T = \begin{pmatrix}\delta \dot{B}_{\parallel} & \delta B_{\perp}\end{pmatrix}$ (6).

$$\overline{\boldsymbol{A}}_b = \left(\boldsymbol{I} - \boldsymbol{1}\left(\boldsymbol{1}^{\mathrm{T}} \boldsymbol{Q}_{\varphi}^{-1} \boldsymbol{1}\right)^{-1} \boldsymbol{1}^{\mathrm{T}} \boldsymbol{Q}_{\varphi}^{-1}\right) \boldsymbol{A}_b \quad (7).$$

$$\boldsymbol{T} = \begin{pmatrix} 0 & \sin(\theta_0) & 0 & -\cos(\theta_0) \\ \cos(\theta_0) & 0 & \sin(\theta_0) & 0 \end{pmatrix} \quad (8)$$

$$\theta_0 := \frac{\bar{\theta}_0 + \bar{\theta}_1}{2} \quad (9)$$

$$\hat{\sigma}_0^2 = \frac{\mathrm{v}_{\varphi}^{\mathrm{T}} \boldsymbol{Q}_{\varphi}^{-1} \mathrm{v}_{\varphi}}{n_{\varphi} - u} \quad (10)$$

2.2. Network Adjustment

The sequential approach of network adjustment combines individual estimation of baseline error with a subsequent adjustment of misclosures between baseline errors. Functional model [15]:

$$E\left\{\begin{pmatrix} \vdots \\ \hat{\mathrm{b}}_{\theta,k} \\ \vdots \end{pmatrix}\right\} = \begin{pmatrix} \cdots & \cdots & \cdots & \cdots & \cdots \\ \boldsymbol{0} & -\mathrm{I}_2 & \boldsymbol{0} & \mathrm{I}_2 & \boldsymbol{0} \\ \cdots & \cdots & \cdots & \cdots & \cdots \end{pmatrix} \begin{pmatrix} \vdots \\ \mathrm{x}_{s,i} \\ \vdots \\ \mathrm{x}_{s,j} \\ \vdots \end{pmatrix} \quad (11)$$

$\boldsymbol{I}_2$ is a 2×2 identity matrix.

Stochastic model:

$$D\{\mathrm{I}_s\} = \varsigma_s^2 \boldsymbol{P}_s^{-1} = \varsigma_s^2 \mathrm{I}_n \otimes \begin{pmatrix} \left(\delta \dot{B}_{\parallel,2\pi}\right)^2 & 0 \\ 0 & \left(\delta \dot{B}_{\parallel,2\pi}\right)^2 \end{pmatrix} \quad (12)$$

Where $\otimes$ is the Kronecker product.

With a datum definition, two zero-mean conditions [15]:

$$\sum_{k=1}^{m} \hat{\mathrm{x}}_{s,k} = \sum_{k=1}^{m} \begin{pmatrix} \delta \hat{x}_{\parallel,s,k} \\ \delta \hat{x}_{\perp,s,k} \end{pmatrix} = \boldsymbol{0} \quad (13)$$

The predicted corrections:

$$\boldsymbol{v}_s = \boldsymbol{A}_s \hat{\boldsymbol{x}}_s - \boldsymbol{l}_s \quad (14)$$

2.3. Quality Control

Baarda [18] data snooping has been widely used in adjustment. Assuming observations are normal distribution. $T_{\phi,i}$ follows a t-distribution [18][19].

$$T_{\phi,i} = \frac{v_{\phi,i}}{\bar{\sigma}_0^2 \sqrt{e_i^T \boldsymbol{Q}_{v_\phi} e_i}} \sim t_{n_\phi - u - 1} \quad (15)$$

$\boldsymbol{Q}_{\boldsymbol{v}_\phi}$ is the cofactor matrix of the corrections $\boldsymbol{v}_\phi = \left(v_{\phi,i}\right)$:

$$\boldsymbol{Q}_{v_\phi} = \boldsymbol{Q}_\phi - \overline{\boldsymbol{A}}_b \boldsymbol{T}^{\mathrm{T}} \boldsymbol{Q}_{\hat{x}\hat{x}} \boldsymbol{T} \overline{\boldsymbol{A}}_b^{\mathrm{T}} \quad (16)$$

When $T_{\phi,i}$ exceeds a dedicated threshold, the ith observation is rejected. The procedure is repeated until all test statistics fall below the threshold.

3. EXPERIMENT AND RESULT

3.1. Research Area and Data

As Los Angeles area (see Figure 2) has dense GPS observations from Southern California Integrated GPS Network (see Figure 3), it has been used frequently to test InSAR techniques. Besides, this area has moderate moving and low image decorrelation [9][20][21][13][22]. Envisat satellite is equipped with ASAR and MERIS sensors to get SAR data and atmospheric water vapor data. We choose a set of m=24 Envisat acquisitions from a scence in Los Angeles (tack 170, frame 2925) between October 6, 2007 and September 25, 2010. Topographic height variations have been accounted for with a 3'' DEM product from the Shuttle Radar Topography Mission (SRTM). All interferograms have been multilooked by a factor 2 in range and 10 in azimuth, yielding pixels of approximately 40m×40m.

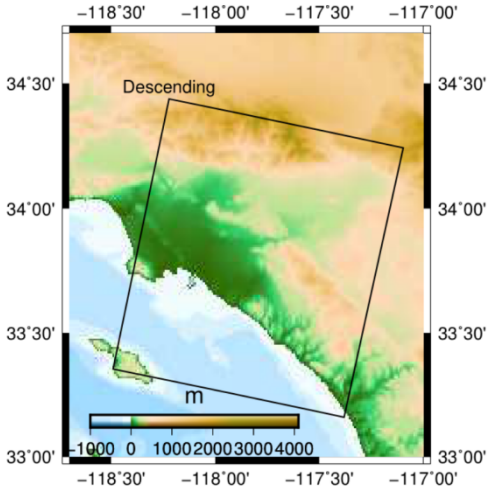

Figure 2 Location and Topography of Research Area

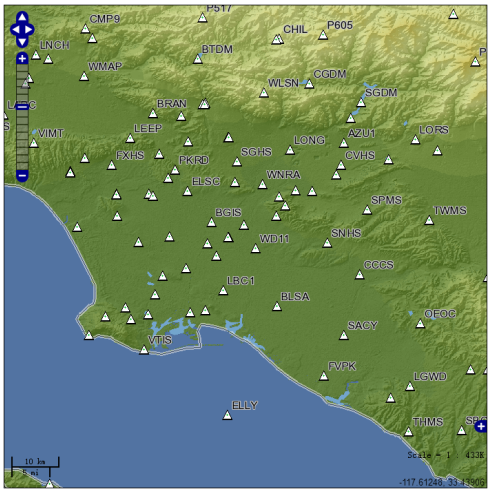

Figure 3 SCIGN

3.2. Data Processing

A network of n=99 interferograms has been set up with a maximum perpendicular baseline of 300 m and a maximum temporal baseline of 500 days. Selection of interferograms and network graph is showed in Figure4 and Figure5 respectively.

Images are sorted and numbered in chronological order. Then interferograms are combined with the expression of master and slave number (see Table 1 and Table 2).

Initial baselines are calculated through precise orbit state vectors. To prevent leverage effect, Ground Control Points (GCP) with high coherence (0.8~1) and uniform distribution has been selected (see Figure 6). Unwrapped differential phase of these GCPs has been used to reestimate baseline, we regard the difference of two baseline value as baseline error.

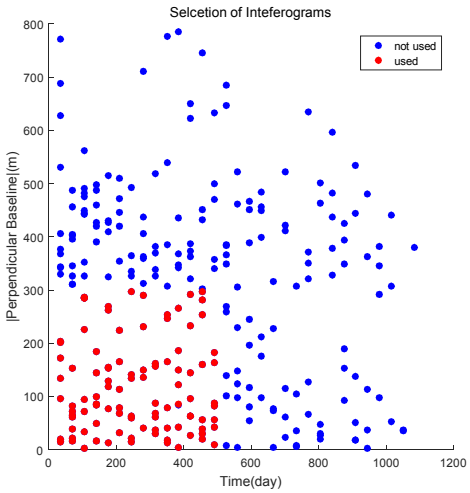

Figure 4 Selection of Interferograms

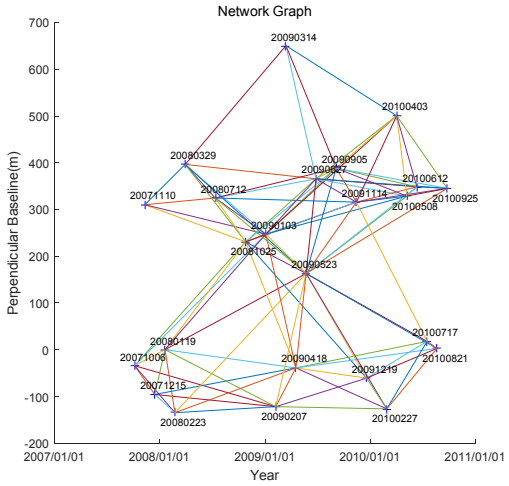

Figure 5 Network Graph

Table 1 Number of Image

Time of Image	Number of Image
20071006	1
20071110	2
20071215	3
20080119	4
20080223	5
20080329	6
20080712	7
…	…
20100925	24

Table 2 Inteferograms Combination

Master Number	Slave Number
1	3
1	4
1	5
1	8
1	9
1	10
2	6
…	…
22	23

3.3. Network Adjustment

Based on the methodology in section 2.2, the functional model of this experiment is:

$$E\left\{\begin{pmatrix}\delta\dot{B}_{\parallel,1}\\ \delta B_{\perp,1}\\ \delta\dot{B}_{\parallel,2}\\ \delta B_{\perp,2}\\ \vdots\\ \delta\dot{B}_{\parallel,99}\\ \delta B_{\perp,99}\end{pmatrix}\right\}=\begin{pmatrix}1&0&0&0&-1&0&0&0&&&\\ 0&1&0&0&0&-1&0&0&&\cdots&\\ 1&0&0&0&0&0&-1&0&&&\\ 0&1&0&0&0&0&0&-1&&&\\ &&&&&&&&\ddots&&\\ \vdots&&&&&&&&1&0&-1\\ &&&&&&&&0&1&0\end{pmatrix}\begin{pmatrix}\delta\dot{x}_{\parallel,s,1}\\ \delta x_{\perp,s,1}\\ \delta\dot{x}_{\parallel,s,2}\\ \delta x_{\perp,s,2}\\ \vdots\\ \delta\dot{x}_{\parallel,s,24}\\ \delta x_{\perp,s,24}\end{pmatrix}$$

(17)

Solving this equation, we get the estimated value of baseline components and orbital error:

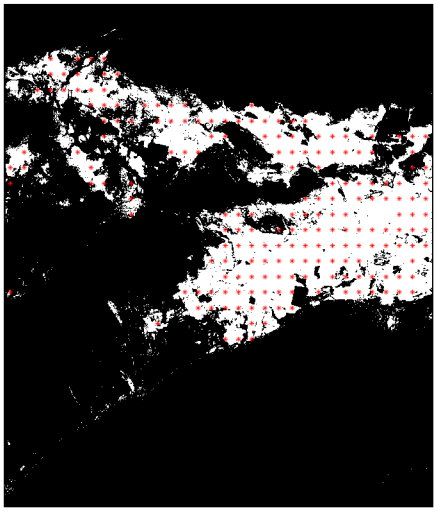

Figure 6 Coherence and GCP(red *)

$$\boldsymbol{b}_{\theta,k}=\begin{Bmatrix}0.0106\\ -0.0729\\ 0.0042\\ -0.1381\\ 0.0303\\ -0.1080\\ 0.0102\\ -0.2573\\ \vdots\\ -0.0168\\ 0.0490\end{Bmatrix}\qquad \boldsymbol{x}_{s,i}=\begin{Bmatrix}0.0183\\ -0.1501\\ -0.0073\\ -0.1002\\ 0.0012\\ -0.0650\\ 0.0085\\ -0.0167\\ \vdots\\ 0.0027\\ 0.1181\end{Bmatrix}$$

With data snooping, two values are detected and rejected (see Figure7). Orbit errors are complementarily quantified in terms of the total number of fringes that they induce into an interferogram ($\delta\dot{B}_{\parallel,2\pi}$=1.7mm/s, $\delta B_{\perp,2\pi}$=26cm):

$$\begin{aligned}\delta\hat{B}_{\mathrm{fr}}&:=\left|\frac{\delta\hat{B}_{\parallel}}{\delta\dot{B}_{\parallel,2\pi}}\right|+\left|\frac{\delta\hat{B}_{\perp}}{\delta B_{\perp,2\pi}}\right|\\ \delta\hat{x}_{\mathrm{fr}}&:=\left|\frac{\delta\hat{x}_{\parallel}}{\delta\dot{B}_{\parallel,2\pi}}\right|+\left|\frac{\delta\hat{x}_{\perp}}{\delta B_{\perp,2\pi}}\right|\\ vB_{\mathrm{fr}}&:=\left|\frac{v\dot{B}_{\parallel}}{\delta\dot{B}_{\parallel,2\pi}}\right|+\left|\frac{vB_{\perp}}{\delta B_{\perp,2\pi}}\right|\end{aligned}\qquad (18)$$

The result of network adjustment is showed in Table3.

Table 3 Result of Network Adjustment

	$d\hat{\dot{B}}_{\parallel}$	$d\hat{B}_{\perp}$	$\delta\hat{B}_{\mathrm{fr}}$	$\delta\hat{\dot{x}}_{\parallel}$	$\delta\hat{x}_{\perp}$	$\delta\hat{x}_{\mathrm{fr}}$	$v_{\hat{\dot{B}}_{\parallel}}$	$v_{B_{\perp}}$	vB_{fr}
	mm/s	cm	fr.	mm/s	cm	fr.	mm/s	cm	fr.
Me1	0.15	-1.08	0.12	0	0	0	-0.22	0.12	0.13
Ma1	40.47	35.22	25.18	18.20	15.82	11.31	17.11	16.43	10.69
Me2	0.42	-0.95	0.28	0	0	0	-0.38	-0.14	0.23
Ma2	40.47	35.22	25.18	18.32	13.94	11.31	13.47	7.74	8.23

Here, Me1 and Ma1 represent the mean and max value before data snooping, and Me2 and Ma2 represent the mean and max value after data snooping. The max value is improved through data snooping. Orbital error before and after data snooping is illustrated in Figure 8, with rejected two interferograms (green line in Figure 8).

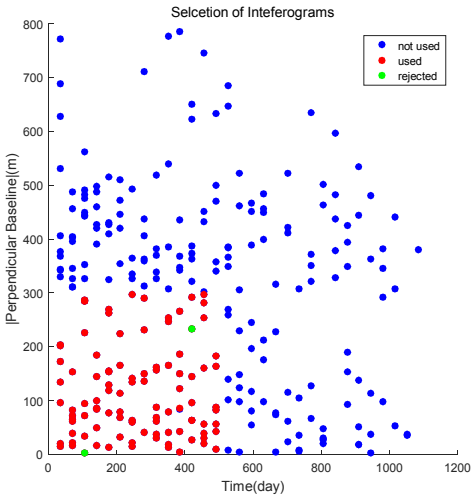

Figure7 Rejected points

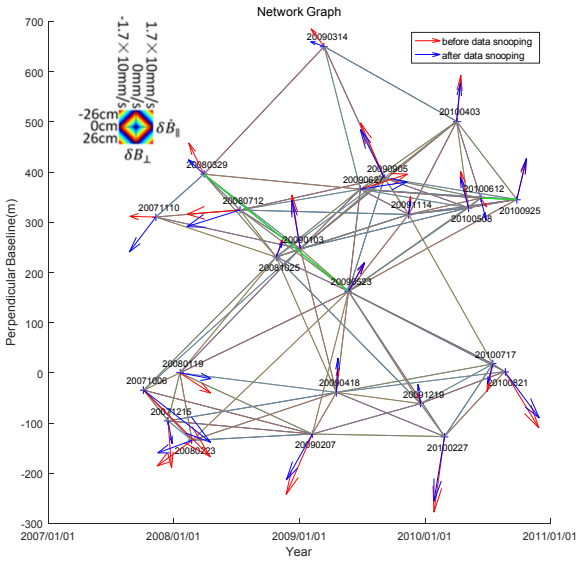

Figure 8 Orbital Error Before and After Data Snooping

4. CONCLUSIONS

This paper mainly focuses on the modeling and analysis of orbital error in spaceborne InSAR, least square and network adjustment are applied in calculating baseline error and orbital error. For quality control, iterative data snooping has proven its capability and reliability to detect and reject outliers. Envisat ASAR data in Los Angeles has the advantages in validating the experiment results. Some more works need doing to indicate the validity of modeling and analysis of orbital error in spaceborne InSAR.

5. ACKNOWLEDGEMENTS

The Envisat Advanced Synthetic Aperture Radar data over the Los Angeles Basin are copyrighted by the European Space Agency (ESA) and provided by Eolisa. The three-arc-second SRTM DEM has been downloaded free of charge from http:// srtm.csi.cgiar.org. One figure was prepared by using Generic Mapping Tools software [23]. This work was supported by the following research projects: the Science and Technology Project Funding of State Grid Corporation (GCB17201700121); the National Natural Science Foundation of China (41304012, 61427802, NSFC41330634, 41374016); the State Key Fund Support of Geodesy and Geodynamics Laboratory (SKLGED2013-4-8-E); the Fundamental Research Funds for the Central Universities (2652015180).

6. REFERENCES

[1] Zhong L, Daniel D, Juliet B, et al. Ground surface deformation patterns, magma supply, and magma storage at Okmok volcano, Alaska, from InSAR analysis: 1. Intereruption deformation, 1997–2008[J]. *Journal of Geophysical Research Solid Earth*, 2010, 115(B5):3040-3040.

[2] Ferretti A, Prati C, Rocca F L. Permanent scatterers in SAR interferometry. IEEE Trans Geosci Remot Sen[J]. *IEEE Transactions on Geoscience & Remote Sensing*, 2001, 39(1):8-20.

[3] Ferretti A, Fumagalli A, Novali F, et al. A New Algorithm for Processing Interferometric Data-Stacks: SqueeSAR[J]. *IEEE Transactions on Geoscience & Remote Sensing*, 2011, 49(9):3460-3470.

[4] Hooper A, Bekaert D, Spaans K, et al. Recent advances in SAR interferometry time series analysis for measuring crustal deformation[J]. *Tectonophysics*, 2012, s 514–517(1):1-13.

[5] Berardino P, Fornaro G, Lanari R, et al. A new Algorithm for Surface Deforamtion Monitoring based on Small BAseline Differential SAR Interferograms[J]. *IEEE Transactions on Geoscience & Remote Sensing*, 2002, 40(11):2375-2383.

[6] Graham L C. Synthetic interferometer radar for topographic mapping[J]. *Proceedings of the IEEE*, 1974, 62(6): 763-768.

[7] Massonnet D, Feigl K L. Radar interferometry and its application to changes in the Earth's surface[J]. *Reviews of Geophysics*, 1998, 36(4):441–500.

[8] Li F K, Goldstein R M. Studies of multi-baseline spaceborne interferometric synthetic aperture radars[J]. *IEEE Transactions on Geoscience & Remote Sensing*, 1990, 28(1):88-97.

[9] Biggs J, Wright T, Lu Z, et al. Multi-interferogram method for measuring interseismic deformation: Denali Fault, Alaska[J]. *Geophysical Journal International,* 2007, 170(3):1165-1179.

[10] Wang T, Jonsson S. Phase-Ramp Reduction in Interseismic Interferograms From Pixel-Offsets[J]. *IEEE Journal of Selected Topics in Applied Earth Observations & Remote Sensing*, 2014, 7(5):1709-1718.

[11] Pepe A, Berardino P, Bonano M, et al. SBAS-Based Satellite Orbit Correction for the Generation of DInSAR Time-Series: Application to RADARSAT-1 Data[J]. *IEEE Transactions on Geoscience & Remote Sensing*, 2011, 49(12):5150-5165.

[12] Bähr H, Hanssen R F. Reliable estimation of orbit errors in spaceborne SAR interferometry[J]. *Journal of Geodesy*, 2012, 86(12):1147-1164.

[13] Zhang L, Ding X, Lu Z, et al. A Novel Multitemporal InSAR Model for Joint Estimation of Deformation Rates and Orbital Errors[J]. *IEEE Transactions on Geoscience and Remote Sensing*, 2014, 52(6): 3529-3540.

[14] Liu G, Hanssen R F, Guo H, et al. Nonlinear Model for InSAR Baseline Error[J]. *IEEE Transactions on Geoscience and Remote Sensing*, 2016, 54(9): 5341-5351.

[15] Bähr H. Orbital Effects in Spaceborne Synthetic Aperture Radar Interferometry[M]. *KIT Scientific Publishing*, 2013.

[16] Small D, Werner C, Nuesch D. Baseline modelling for ERS-1 SAR interferometry[C]// Geoscience and Remote Sensing Symposium, 1993. IGARSS '93. Better Understanding of Earth Environment., *International. IEEE*, 1993:1204-1206 vol.3.

[17] Hanssen R F. Radar Interferometry Data Interpretation and Error Analysis[J]. *Journal of the Graduate School of the Chinese Academy of Sciences*, 2001, 2(1):V5-577-V5-580.

[18] Baarda W. A testing procedure for use in geodetic networks.[J]. *Delft Kanaalweg Rijkscommissie Voor Geodesie*, 1968, -1.

[19] Peng J. Jointly Robust Estimation of Unknown Parameters and Variance Components Based on Expectation-Maximization Algorithm[J]. *Journal of Surveying Engineering*, 2009, 135(1):1-9.

[20] Lanari R, Lundgren P, Manzo M, et al. Satellite radar interferometry time series analysis of surface deformation for Los Angeles, California[J]. *Geophysical Research Letters*, 2004, 31(23):345-357.

[21] Colesanti C, Ferretti A, Novali F, et al. SAR monitoring of progressive and seasonal ground deformation using the permanent scatterers technique[J]. *IEEE Transactions on Geoscience & Remote Sensing,* 2003, 41(7):1685-1701.

[22] Hu J, Ding X L, Li Z W, et al. Vertical and horizontal displacements of Los Angeles from InSAR and GPS time series analysis: resolving tectonic and anthropogenic motions[J]. *Journal of Geodynamics*, 2016, 99:27-38.

[23] Wessel P, Smith W H F. New, improved version of generic mapping tools released[J]. *Eos Transactions American Geophysical Union*, 1998, 79(47):579-579.

View publication stats